

Storage-less and Converter-less Photovoltaic Energy Harvesting with Maximum Power Point Tracking for Internet of Things

Yiqun Wang, *Student Member, IEEE*, Yongpan Liu, *Member, IEEE*, Cong Wang, Zewei Li, Xiao Sheng, Hyung Gyu Lee, *Member, IEEE*, Naehyuck Chang, *Fellow, IEEE*, Huazhong Yang, *Senior Member, IEEE*

Abstract—Energy harvesting from natural environment gives range of benefits for the Internet of Things. Scavenging energy from photovoltaic (PV) cells is one of the most practical solutions in terms of power density among existing energy harvesting sources. PV power systems mandate the maximum power point tracking (MPPT) to scavenge the maximum possible solar energy. In general, a switching-mode power converter, an MPPT charger, controls the charging current to the energy storage element (a battery or equivalent), and the energy storage element provides power to the load device. The mismatch between the maximum power point (MPP) current and the load current is managed by the energy storage element. However, such architecture causes significant energy loss (typically over 20%) and a significant weight/volume and a high cost due to the cascaded power converters and the energy storage element.

This paper pioneers a converter-less PV power system with the MPPT that directly supplies power to the load without the power converters or the energy storage element. The proposed system uses a nonvolatile microprocessor to enable an extremely fine-grain dynamic power management (DPM) in a few hundred microseconds. This makes it possible to match the load current with the MPP current. We present detailed modeling, simulation and optimization of the proposed energy harvesting system including the radio frequency transceiver. Experiments show that the proposed setup achieves an 87.1% of overall system efficiency during a day, 30.6% higher than the conventional MPPT methods in actual measurements, and thus a significantly higher duty cycle under a weak solar irradiance.

Index Terms—Energy harvesting, Photovoltaic systems, Maximum-power-point tracking (MPPT), Energy efficiency, Storage-less and converter-less

I. INTRODUCTION

Some technical reports predicted that the number of smart sensors will reach to trillions in the near future [1]. Battery maintenance of the sensors becomes a severe problem both in time and costs in such a sensor-abundant world. Energy harvesting is a promising alternative to the batteries, especially in the applications of biomedical sensing, body area sensors, and health monitoring [2, 3]. There are various energy scavenging technologies that are able to power the sensors from optical, kinetic, thermal, radio frequency energy, and so forth. Among

them, photovoltaic (PV) energy is one of the most promising ones thanks to power density, efficiency and the range of the output voltage and current [4].

The output characteristics of a PV cell vary nonlinearly by temperature and solar irradiance. PV cells have a much higher output impedance compared with batteries, and thus PV energy harvesting systems mandate the maximum power point tracking (MPPT) to avoid majority of solar energy is dissipated in the PV cells. The MPPT is not only important for large-scale solar farms but critical for milliwatt or even sub-milliwatt sensor node systems [5, 6]. There are two major factors that differentiate the MPPT quality: i) the efficiency of MPPT strategy and ii) the efficiency of the power conversion circuit. The fractional open-circuit voltage (FVoc) MPPT strategy, which exploits the nearly linear relationship between the PV panel open-circuit voltage and the voltage at maximum power point (MPP), is most preferred for its low computation complexity and low power components [7]. Perturb and observe (P&O) strategies requires more complex circuits for power measurement, which are appropriate for relatively high power (> 50W) system [8] to come up with more elaborated and precise MPPT.

High efficient power conversion circuits are strongly desired in low-voltage energy harvesting systems [9, 10]. In a PV energy harvesting system, a DC-DC converter is necessary to keep the operation point of PV cell to the MPP, and it isolates the PV cell voltage from the terminal voltage of energy storage. The PV cell MPP voltage varies significantly, which makes it difficult to maintain a high efficiency of power converters between the PV cells and batteries. It goes without saying that switching-mode DC-DC converters with high efficiency are highly desirable. Pulse width modulation (PWM) control is common for high-power applications [6]. However, PWM control exhibits a poor conversion efficiency at a light load due to the switching loss. Pulse frequency modulation (PFM) control is an alternative way to maintain a high efficiency at a light load at the expense of a higher ripple [11]. The dual-mode control methods switching between the PWM and PFM mode by the load current, is desirable to maintain a high efficiency even in a low-power PV energy harvesting system.

Although the MPPT strategies and converter control methods are different dimension of problems in a PV energy harvesting system, a low-power PV system can be generally abstracted to a typical architecture shown in Fig. 1. The architecture has three stages; The MPP tracking stage includes

Y. Wang, Y. Liu, C. Wang, Z. Li, X. Sheng, and H. Yang are with the Department of Electronic Engineering, Tsinghua University, Beijing, 100084, China (e-mail: {ypliu, yanghz}@tsinghua.edu.cn; {wang-yq05, shengxiao12, lizw13}@mails.tsinghua.edu.cn; cong.wang@aliyun.com)

N. Chang is with the Department of Electrical Engineering and Computer Science, Seoul National University, Seoul, Korea (e-mail: naehyuck@elpl.snu.ac.kr)

H. G. Lee is with Daegu University, Gyeongsan 712-714, South Korea (e-mail: hglee@daegu.ac.kr)

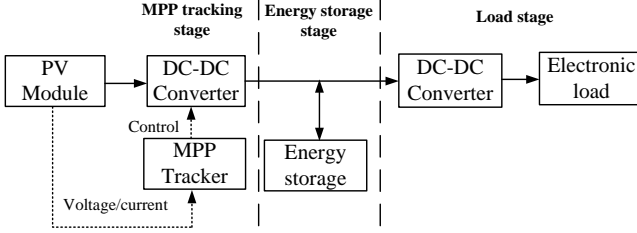


Fig. 1. Typical architecture of a PV power system with MPPT [5].

an MPP tracker and a DC-DC converter. The MPP tracker implements the MPPT strategy measuring the current and voltage of the PV cell and set the DC-DC converter to either PFM or PWM control mode.

The second stage is the energy storage that performs a charge buffer to bridge the mismatch between the PV source current and load current by charging or discharging. The energy storage is a supercapacitor or a battery, or in a hybrid form [12]. In the low-power PV energy harvesting systems, the supercapacitor is more preferred because it has superior characteristics to batteries in terms of cycle efficiency and cycle life [13, 14]. Therefore, this paper adopts a supercapacitor as the energy storage. The third stage, the load stage, includes another DC-DC converter as a load regulator that generates a proper voltage for the load device.

Therefore, a PV power system requires two cascaded DC-DC converters and supercapacitors without doubt. However, there are several disadvantages of the cascaded DC-DC converters and supercapacitors though they are mandatory to make the system functional. First, the DC-DC converters have non-negligible conversion loss. The efficiency of the DC-DC converter varies in a wide range (60% – 90%) when the voltage gap between the PV cell and the supercapacitor changes [15]. It is hard to guarantee a high efficiency around the clock because the voltage of the supercapacitor is fluctuant in a wide range. Second, the supercapacitor suffers from non-ideal characteristics such as self-discharge (1mW for a 10F supercapacitor at 2V [16]), charge distribution and non-ideal cycle efficiency [6, 17], which cause non-trivial energy loss in a milliwatt low power PV system. Moreover, the unstable terminal voltage of supercapacitors further degrades the efficiency of DC-DC converter. Third, the inductor based converters and the large size of supercapacitors jointly increase the form factor of the PV energy harvesting system and impede on-chip integration. Above three factors seriously discourage deployment of small, power-efficient and self-sustainable smart sensors in various applications.

Removal of the DC-DC converters and supercapacitors gives a great freedom in size, cost, volume, and so forth. However, there are obvious obstacles in such a radical approach. First, the voltage and current of the electronics load device should be exactly matched with the MPP voltage and current of PV cells, which requires fine-grained dynamic power management (DPM). Some works provide load-matching task scheduling algorithms on the electronic load to achieve high energy efficiency [18, 19]. However, their algorithms cannot track MPP without the DC-DC converters and battery. Second, without the energy storage, the electronics load should have

high resilience to power interrupt when the solar irradiance is too weak to support the system. In order to provide enough energy for system data retention under power failures, Brunelli et al. [20] have adopt a large capacitor with hundreds of microfarads, which suffers from large capacitor area and potential self-discharge.

We propose a storage-less and converter-less PV power system that performs the MPPT, with low circuit complexity and high energy efficiency. Thanks to the development of nonvolatile microprocessor, we only use a small capacitor of tens of microfarad for signal integrity and achieve a millisecond fine-grain DPM. The DC-DC converter is replaced by a DPM controlled load switch to maintain the MPP. Without the DC-DC converter in the load stage, the PV cell acts like a regulated voltage source as long as the MPP is tracked. Fast enough DPM makes the output voltage of PV module swing in a very small range around MPP, which is essential to achieve high energy efficiency. Specially, we make the following contributions:

- 1) We propose the architecture and fine-grained DPM working mechanism of the storage-less and converter-less PV power system. By removing the power converters and integrating the nonvolatile processor, the proposed system achieves much lower circuit complexity and higher energy efficiency than conventional MPPT system.
- 2) We set up the component models of the proposed system. Furthermore, a mathematical model of system efficiency is given. These models are validated by measurements on an actual system prototype.
- 3) We provide some design guidelines of the critical system components, including the PV module and capacitors. Moreover, we provide a hybrid MPPT window tuning method to speed up the MPP tracking and optimize the system efficiency.
- 4) The simulation results show that the proposed system achieves an overall system efficiency of 87.1% and executes 3.4X more tasks than baseline systems in one day. The measurement results demonstrate that the proposed PV power system achieves 30.6% higher system efficiency than a baseline MPPT system with DC-DC converters and supercapacitors.

The remainder of this paper is organized as follows: Section II describes the architecture and working mechanism of the proposed converter-less PV power system. Section III and Section IV provide the models of system components and overall system efficiency. Section V proposes some design guidelines and system optimization methods based on the system models. The system models are validated in Section VI by an implemented system prototype. Section VII shows the experimental results, and Section VIII concludes this paper.

II. STORAGE-LESS AND CONVERTER-LESS PV SYSTEM

This section first describes the architecture of the proposed storage-less and converter-less PV power system with MPPT. We then discuss the DPM based system working sequence in detail. In the end, we give the definition of system efficiency of the proposed PV system.

A. System Architecture

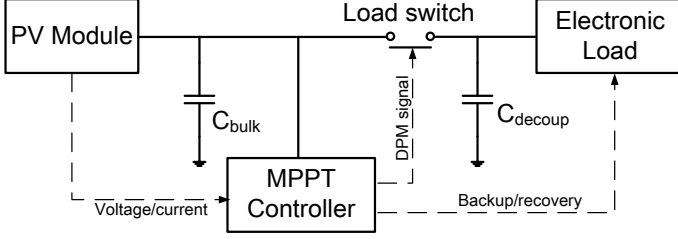


Fig. 2. Proposed converter-less PV system architecture with MPPT.

The storage-less and converter-less PV power system is shown in Fig. 2. There are four major components: the PV module, the electronic load, the load switch, and the MPPT controller. The PV module is carefully selected so that its MPP voltage is close to the legal operating voltage of the electronic load. It is easy to customize MPP voltage by stacking a different number of low voltage PV cells in serial [21]. On the load side, we use a nonvolatile microprocessor based electronic load, which has microseconds sleep and wake-up time and very few energy overheads. The PV module and the electronic load are connected via a load switch. The MPPT controller is responsible to 1) track the MPP of PV module according to its voltage and current by providing a dynamic-power-management (DPM) signal to the load switch 2) control the backup and recovery of the electronic load. The MPPT controller is implemented with discrete circuits or a micro-controller.

Additionally, there is a bulk capacitor C_{bulk} connected in parallel with the PV module. It extends the time constant of the PV module so that the time constant may match with the feasible DPM period of the load devices. There is a decoupling capacitor C_{decoup} on the load side, which maintains the power integrity of the electronic load. Because the nonvolatile processor based electronic load has fast and energy efficient backup and recovery mechanism, there is no need to store much energy on C_{bulk} and C_{decoup} . Therefore, the size of the capacitors can be small enough to support fine-grained DPM and reduce self-leakage. In the following, the working sequence of the proposed system is described in detail.

B. Working Sequence

The proposed PV power system achieves MPPT with fine-grained DPM on the electronic load. The MPPT controller provides a DPM signal to continuously turn on and off the load switch. It forces the PV module output voltage, V_{pv} , to fluctuate around the MPP voltage, V_{mpp} , by modulating the DPM signal (see in Fig. 3(a)). The waveform of V_{pv} in one DPM cycle is illustrated in Fig. 3(b). V_{pv} is maintained within a small window, $[V_l, V_h]$, around V_{mpp} . The system working sequence in one DPM cycle is mainly departed to two stages: the “OFF” stage and the “ON” stage. Once V_{pv} becomes lower than V_l , the MPP controller turns off the load switch to shut down the electronic load, and the system enters the “OFF” stage. After that, the PV module charges the bulk capacitor and the V_{pv} begins to rise. After V_{pv} reaches to V_h , the system

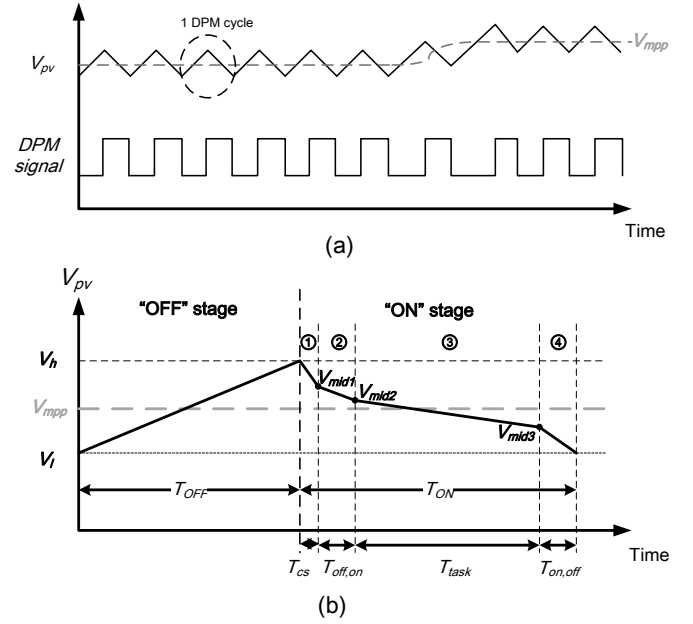


Fig. 3. (a) Maximum power point tracking by adjusting the DPM signal (b) PV module output voltage and related system working sequence in one DPM cycle. The “ON” stage contains four processes: ① Charge sharing, ② OFF-to-ON transition, ③ Task execution, and ④ ON-to-OFF transition.

switches to the “ON” stage. The MPPT controller turns on the load switch and wakes up the electronic load. Then, the PV module output voltage drops as the load is connected to the PV module. (We only consider the condition that the load current is larger than the MPP current, otherwise, the PV module is over-designed.) The “ON” stage can be divided into four processes, and described in the following:

- **Charge sharing:** After the load switch is turned ON, the bulk capacitor shares the charge with the decoupling capacitor at the output stage, resulting in a voltage drop of the bulk capacitor from V_h to V_{mid1} . The charge sharing process lasts for a short time T_{cs} .
- **OFF-to-ON transition:** After the charge sharing process, the power supply of the electronic load recovers, and the system goes into OFF-to-ON transition process. It restores the status from nonvolatile memories and prepares to continue the normal task execution. The OFF-to-ON transition time is $T_{off,on}$. When the OFF-to-ON transition finishes, the V_{pv} drops to V_{mid2} .
- **Task execution:** Once the OFF-to-ON transition is over, the electronic load goes into normal operation and start executing its tasks. The task execution process lasts until MPPT controller provides a backup signal to the electronic load. We denote the time of the task execution process as T_{task} . When the task execution process finishes, the V_{pv} drops to V_{mid3} .
- **ON-to-OFF transition:** The MPPT controller keeps monitoring the voltage drop of V_{pv} during the task execution time. When V_{pv} becomes close to V_l , the MPPT controller generates the backup signal and forces the load to backup its states and prepare to be turned off. The ON-to-OFF transition process is reserved for system states backup before turning OFF the load switches. The ON-to-OFF transition time is denoted as $T_{on,off}$.

C. System efficiency

As described above, the DPM based MPPT is not ideal for solar energy utilization. First, the output voltage of PV module cannot always maintain the MPP voltage, but swings around the MPP voltage, which makes the MPPT non-ideal. Second, the charge sharing and state transition processes waste energy, which makes the energy transfer non-ideal. The above non-ideal factors render us to consider the system efficiency of the total PV system, which indicates how much solar energy is effectively used.

We consider that the effective energy is for task execution. Therefore, the system efficiency is defined as the ratio of task execution energy to the total energy generated at the maximum power point. We first give the definition of system efficiency in one DPM cycle:

$$\eta_{sys} = \frac{E_{task}}{E_{mpp}} = \frac{P_{task}T_{task}}{P_{mpp}(T_{ON} + T_{OFF})} = \frac{P_{task}T_{task}}{P_{mpp}T_{dpm}}, (P_{mpp} < P_{task}), \quad (1)$$

where E_{task} is the effective energy for task execution, and P_{task} is the average task execution power of electronic load. P_{mpp} and E_{mpp} are the maximum power and maximum energy that can be extracted from the PV module in a DPM cycle. T_{ON} , T_{OFF} and T_{task} denote the time of “ON” stage, “OFF” stage and task execution process shown in Figure 3(b). T_{dpm} is the time of one DPM cycle, which is equal to $(T_{ON} + T_{OFF})$. We only consider the situation that $(P_{mpp} < P_{task})$, because if $(P_{mpp} > P_{task})$, the load switch is always connected and the output power of PV module are forced to P_{task} rather than tracking the MPP.

We can also give the definition of system efficiency during a long period with N DPM cycles as:

$$\eta_{sys,N} = \frac{\sum_{i=1}^N E_{task,i}}{\sum_{i=1}^N E_{mpp,i}} = \frac{\sum_{i=1}^N P_{task,i}T_{task,i}}{\sum_{i=1}^N P_{mpp,i}(T_{ON,i} + T_{OFF,i})}, \quad (2)$$

where the symbols with subscript $[*]_{*,i}$ indicate the related parameter in the i -th DPM cycle.

From (1), we can see that the system efficiency is determined by five parameters: P_{task} , P_{mpp} , T_{ON} , T_{OFF} and T_{task} . Although P_{task} and P_{mpp} can be obtained directly from the models of electronic load and PV module, the T_{ON} , T_{OFF} and T_{task} are not easy to calculate, which is related to the time of charging, discharging and ON-OFF transitions. In the following section, we will give the models of the major system components. Then we derive the mathematical expression of system efficiency from the models.

III. COMPONENT MODELS

In this section, we provide the models of major components in the proposed PV system, including the PV module, the nonvolatile microprocessor based electronic load, the MPPT controller and the load switch.

A. Photovoltaic model

The PV module impacts the system efficiency via output voltage and current, as well as the MPP characteristics. In order to establish their relationships, we use a well-known single diode model [22], shown in Fig. 4 to simulate the DC

output of a PV module. The I-V characteristic of a PV module is represented by (3) and (4).

$$I_{pv} = I_L - I_0 \left(e^{\frac{V_{pv} + I_{pv}R_s}{a}} - 1 \right) - \frac{V_{pv} + I_{pv}R_s}{R_{sh}}, \quad (3)$$

$$a \equiv \frac{N_s n_1 k T_c}{q}, \quad (4)$$

where N_s , n_1 , k , T_c and q indicate the number of cells in series, the ideality factor of the diode, the Boltzmann constant, the module temperature, and the electron charge, respectively.

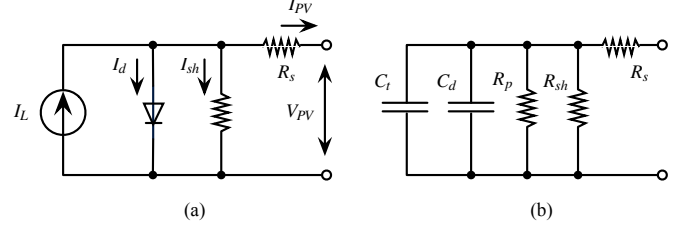


Fig. 4. (a) A DC equivalent circuit of a PV module; (b) An AC equivalent circuit of a PV module.

To determine the relationship between output current I_{pv} and output voltage V_{pv} of a PV module, we need to know the five parameters in (3) and (4), including the light current I_L , the diode reverse saturation current I_0 , the series resistance R_s , the shunt resistance R_{sh} , as well as the ideality factor n_1 .

We extract the five parameters (I_L , I_0 , n_1 , R_s , R_{sh}) with a curve-fitting method. First, we measure a set of voltage-current points under a reference condition (solar irradiance of 200 W/m^2 and temperature of 27°C). Then we find the best-fit parameters that minimize the deviation between the curve provided by the model and the measured points. But these best-fit parameter values are valid only for the reference condition. For other temperature and solar irradiance condition, we can obtain corresponding parameters with (5), (6) and (7) as introduced in [23].

$$I_L = \frac{S}{S_{ref}} [I_{L,ref} + \alpha_{I_{sc}}(T_c - T_{c,ref})], \quad (5)$$

$$\frac{I_0}{I_{0,ref}} = \frac{T_c}{T_{c,ref}} \exp \left[\frac{E_g}{k} \left(\frac{1}{T_c} - \frac{1}{T_{c,ref}} \right) \right], \quad (6)$$

$$\frac{R_{sh}}{R_{sh,ref}} = \frac{S_{ref}}{S}, \quad (7)$$

where S is the solar irradiance in W/m^2 , E_g is the material band gap energy. Symbols with subscript $[*]_{ref}$ are values under reference condition. Besides, we assume that series resistance R_s and diode ideality factor n_1 are independent of temperature and solar irradiance in this study. where S and E_g indicate the solar irradiance in W/m^2 , and the material band gap energy, respectively. Symbols with subscript $[*]_{ref}$ are valued under the reference condition. Following the investigation in [22], the series resistance R_s and diode ideality factor n_1 are independent of temperature and solar irradiance.

Table I lists the five parameters of a PV module extracted from measurement results. As illustrated in Fig. 5(a), the model's value fits well with the actual characteristics of the PV module. To obtain the P_{mpp} , we give the simulation of

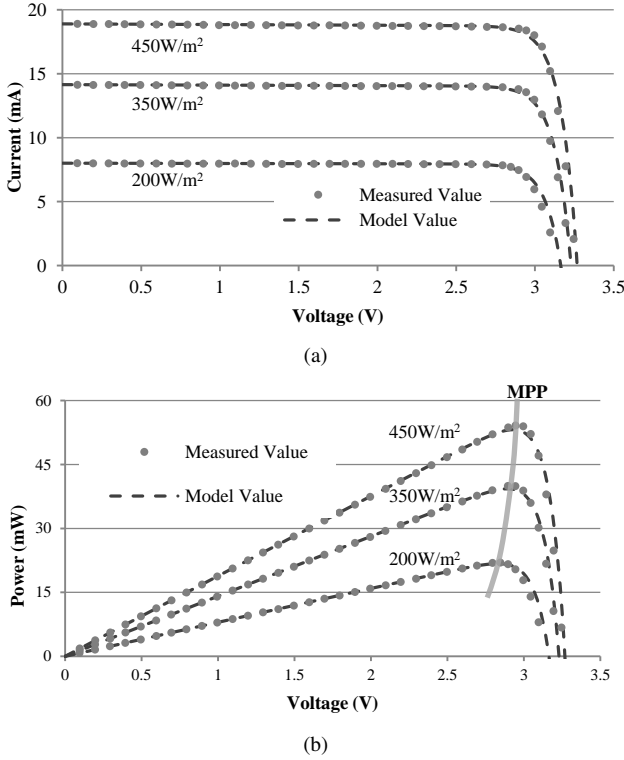


Fig. 5. (a) I-V curve; (b) P-V curve of a $4.5 \times 5.5 \text{ cm}^2$ experimental photovoltaic module under different solar insolation at the temperature of 300K. An MPPT window is shown on the curve for the irradiance of 200 W/m^2 .

TABLE I
MODEL PARAMETERS OF THE EXPERIMENTAL PV MODULE
(TEST CONDITION: $S = 200 \text{ W/m}^2$, $T_c = 300 \text{ K}$).

I_L	I_0	n_1	R_s	R_{sh}	N_s
8.01 mA	$1.01 \cdot 10^{-16} \text{ A}$	1.885	0.17 Ω	22.36k Ω	2

the P-V curve of the PV module from the I-V characteristics, and it is shown in Fig. 5(b). The PV output power P_{pv} is calculated as $P_{pv} = I_{pv} \times V_{pv}$. The MPP is the peak value with zero gradient in the P-V curve, so we have:

$$P_{mpp} = P_{pv} \Big|_{\frac{dP_{pv}}{dV_{pv}}=0} \quad (8)$$

B. Nonvolatile microprocessor based electronic load

The electronic load discussed in this paper is typically a sensor node, which consists of a nonvolatile microprocessor and peripherals including sensors, RF modules, etc. The electronic load impacts the system efficiency via the following parameters:

- $T_{off,on}$: transition time from “OFF” state to “ON” state,
- $T_{on,off}$: transition time from “ON” state to “OFF” state,
- $I_{off,on}$: average current during transition from “OFF” state to “ON” state,
- $I_{on,off}$: average current during transition from “ON” state to “OFF” state,
- I_{task} : average current during task execution,
- P_{task} : average power during task execution.

The transition parameters of the electronic load are dominated by the microprocessor, because the microprocessor has

to backup and recover its register data during the transitions in order to guarantee contiguous working, which leads to a certain amount of data migration. Conventional microprocessor migrates the data from/to a centralized nonvolatile memories, such as Flash (see in Fig 6(a)). The limited bandwidth of the centralized nonvolatile memory causes milliseconds migration time. By contrast, the nonvolatile microprocessor uses a distributed nonvolatile backup mechanism by constructing the register files with nonvolatile flip-flops (see in Fig 6(b)). The nonvolatile flip-flop contains a main flip-flop and local nonvolatile elements. Data migrations between the main flip-flops and their local nonvolatile elements are performed in parallel among the flip-flops, thus expediting the backup and recovery processes. The backup and recovery time of the nonvolatile microprocessor are several micro-seconds, or even hundreds of nanoseconds [24], being three to four orders of magnitude faster than conventional microprocessors.

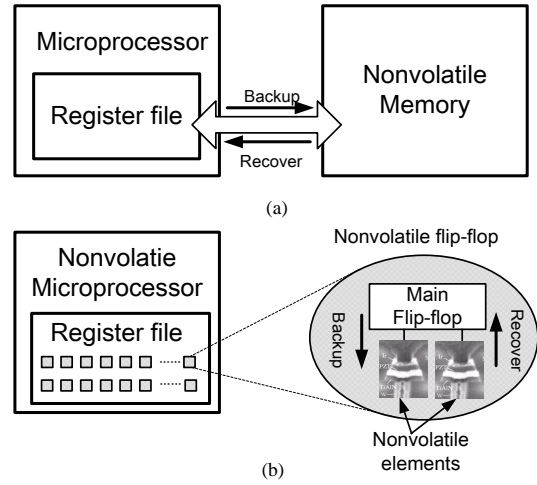


Fig. 6. (a) Data backup and recover architecture for conventional microprocessor; (b) Data backup and recover architecture for nonvolatile microprocessor.

In this paper, we use a fabricated nonvolatile microprocessor named THU1010N [25] as the nonvolatile microprocessor, and the sensor node prototype described in Section VI as the electronic load. Table II summarizes the power consumption and transition overheads of THU1010N and the sensor node. The statistics of the sensor node take into account the overhead of peripherals, in addition to the nonvolatile microprocessor.

TABLE II
SPECIFICATIONS OF THE NONVOLATILE PROCESSOR USED IN THIS PAPER.

Model	$T_{off,on}$	$T_{on,off}$	$I_{off,on}$	$I_{on,off}$	I_{task}	P_{task}
THU1010N	3 μs	7 μs	2.2mA	1.8mA	2.2mA	3.29mW
Electronic load	41 μs	7 μs	9.8mA	1.8mA	12.2mA	40.4mW

C. MPPT controller and load switch

For the MPPT controller, we only consider its current consumption I_{ctrl} . In this paper, we choose a low power FVoc method as the MPPT strategy. The circuit structure is

described in Section VI in detail. From the measurement of the actual prototype, I_{ctrl} is around 300 μA .

We use a simple CMOS transmission gate as the load switch. The equivalent on-resistance of the load switch, R_{ls} , is hundreds of $m\Omega$. The current through the load switch, I_{ls} , is close to the current consumption of electronic load, which is tens of mA . Therefore, the voltage drop on the load switch is around 1 mV , which can be neglected. The power consumption of the load switch, P_{ls} , is tens of μW .

In the following section, we use the component models and corresponding denotations described above to model the system efficiency.

IV. SYSTEM EFFICIENCY

In this section, we derive the system efficiency from component models described above. Afterwards, we give some further analysis on the optimizing factors of the system efficiency.

A. System efficiency derivation

In order to calculate the system efficiency in (1), we mainly focus on solving T_{ON} , T_{OFF} and T_{task} . P_{task} and P_{mpp} can be easily extracted from the component models. The parameters are summarized in Table III, which are also marked in Fig. 3 and Fig. 7.

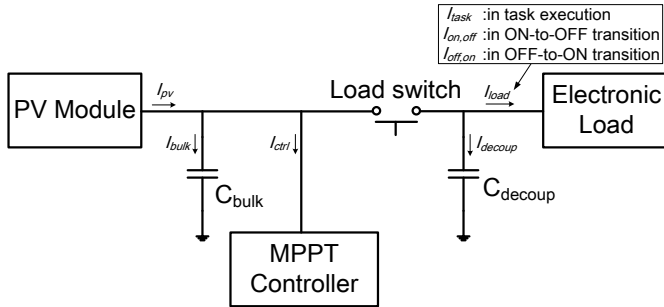


Fig. 7. Current denotation of the proposed PV system.

1) T_{OFF} : In the “OFF” stage, the load switch is disconnected. I_{pv} flows to the MPPT controller and bulk capacitor. With the Kirchhoff’s current law, we have:

$$I_{pv} = I_{ctrl} + I_{bulk} = I_{ctrl} + C_{bulk} \frac{dV_{pv}}{dt}, (I_{pv} > I_{ctrl}). \quad (9)$$

The constraint $I_{pv} > I_{ctrl}$ should be met, or the bulk capacitor cannot be charged. T_{OFF} is the time to charge the bulk capacitor from V_l to V_h :

$$T_{OFF} = \int_{V_l}^{V_h} \frac{C_{bulk}}{I_{pv} - I_{ctrl}} dV_{pv}. \quad (10)$$

2) T_{ON} and T_{task} : In the “ON” stage, the load switch is connected. With the Kirchhoff’s current law, we have:

$$I_{pv} = I_{ctrl} + I_{bulk} + I_{decoup} + I_{load}, (I_{pv} < I_{ctrl} + I_{load}). \quad (11)$$

Because the capacitors are discharged, the constraint $I_{pv} < I_{ctrl} + I_{load}$ should be met, where I_{load} takes different values

TABLE III
SYMBOLS USED IN THE SYSTEM EFFICIENCY DERIVATION.

Symbols	Description
I_{pv}, V_{pv}	The output current and voltage of the PV module.
P_{mpp}	The output power of the PV module at the MPP.
P_{task}	The average power of electronic load during task execution.
I_{load}	The current of electronic load during “ON” stage
I_{task}	The current of electronic load during task execution.
$I_{on,off}$	The current of electronic load during ON-to-OFF transition.
$I_{off,on}$	The current of electronic load during OFF-to-ON transition.
I_{ctrl}	The current consumption of the MPPT controller.
I_{bulk}	The current consumption of the bulk capacitor.
I_{decoup}	The current consumption of the decoupling capacitor.
V_h, V_l	The upper and lower threshold of V_{pv} .
V_{mid1}	Value of V_{pv} at the end of “Charge sharing” process.
V_{mid2}	Value of V_{pv} at the end of “OFF-to-ON transition” process.
V_{mid3}	Value of V_{pv} at the end of “Task execution” process.
V_{bulk}	Terminal voltage of the bulk capacitor.
V_{decoup}	Terminal voltage of the decoupling capacitor.
C_{bulk}	The capacitance of the bulk capacitor.
C_{decoup}	The capacitance of the decoupling capacitor.
T_{ON}, T_{OFF}	Time of “ON” stage and “OFF” stage.
T_{cs}	Time of “Charge sharing” process.
T_{task}	Time of task execution process.
$T_{on,off}$	Time of “ON-to-OFF transition” process.
$T_{off,on}$	Time of “OFF-to-ON transition” process.
R_{ls}	Equivalent on-resistance of the load switch.

during different processes in the “ON” stage (see in Fig. 7). The constraint is met in each process, so it can be written as:

$$I_{pv} < I_{ctrl} + \min\{I_{on,off}, I_{off,on}, I_{task}\} \quad (12)$$

According to the “ON” stage in Fig. 3, T_{ON} can be expressed as:

$$T_{ON} = T_{cs} + T_{on,off} + T_{off,on} + T_{task}, \quad (13)$$

where $T_{on,off}$ and $T_{off,on}$ is extracted from the measured results in Table II. We need calculate T_{cs} and T_{task} in the following paragraphs.

Charge sharing time: The charge sharing process happens instantly after the load switch is connected. The bulk capacitor shares its charge with decoupling capacitor, and finally they reach to the same voltage, V_{mid1} . The sharing charge is proportional to their capacitance, which yields:

$$V_{mid1} = \frac{C_{bulk} V_h}{C_{bulk} + C_{decoup}}. \quad (14)$$

The charge sharing process obeys an exponential feature with the time constant τ defined as:

$$\tau = \frac{C_{bulk} C_{decoup} R_{ls}}{C_{bulk} + C_{decoup}}, \quad (15)$$

where R_{ls} is the equivalent resistance of load switch. It takes infinite time for V_{bulk} and V_{decoup} to be V_{mid1} . We use 5τ as an approximate charge sharing time, since it indicates the charge sharing process completes over 99%.

$$T_{cs} = 5\tau = \frac{5C_{bulk} C_{decoup} R_{ls}}{C_{bulk} + C_{decoup}}. \quad (16)$$

$$\left\{ \begin{array}{l} \eta_{\text{sys}} = \frac{P_{\text{task}} \int_{V_{\text{mid}3}}^{V_{\text{mid}2}} \frac{C_{\text{bulk}} + C_{\text{decoup}}}{I_{\text{ctrl}} + I_{\text{task}} - I_{\text{pv}}} dV_{\text{pv}}}{P_{\text{mpp}} \left(\int_{V_l}^{V_h} \frac{C_{\text{bulk}}}{I_{\text{pv}} - I_{\text{ctrl}}} dV_{\text{pv}} + \frac{5C_{\text{bulk}}C_{\text{decoup}}R_{\text{ls}}}{C_{\text{bulk}} + C_{\text{decoup}}} + \int_{V_{\text{mid}3}}^{V_{\text{mid}2}} \frac{C_{\text{bulk}} + C_{\text{decoup}}}{I_{\text{ctrl}} + I_{\text{task}} - I_{\text{pv}}} dV_{\text{pv}} + T_{\text{on,off}} + T_{\text{off,on}} \right)} \\ V_{\text{mid}2} = \frac{C_{\text{bulk}}V_h}{C_{\text{bulk}} + C_{\text{decoup}}} - \int_0^{T_{\text{off,on}}} \frac{I_{\text{ctrl}} + I_{\text{off,on}} - I_{\text{pv}}}{C_{\text{bulk}} + C_{\text{decoup}}} dt \\ V_{\text{mid}3} = V_l + \int_0^{T_{\text{on,off}}} \frac{I_{\text{ctrl}} + I_{\text{on,off}} - I_{\text{pv}}}{C_{\text{bulk}} + C_{\text{decoup}}} dt. \end{array} \right. \quad (20)$$

Task execution time: As Fig. 3 shows, V_{pv} drops from $V_{\text{mid}2}$ to $V_{\text{mid}3}$ during the stage of task execution. T_{task} equals to the discharging time of bulk capacitor from $V_{\text{mid}2}$ to $V_{\text{mid}3}$. According to the current relationships in (11) and Fig. 7, we have

$$T_{\text{task}} = \int_{V_{\text{mid}3}}^{V_{\text{mid}2}} \frac{C_{\text{bulk}} + C_{\text{decoup}}}{I_{\text{ctrl}} + I_{\text{task}} - I_{\text{pv}}} dV_{\text{pv}}, \quad (17)$$

where $V_{\text{mid}2}$ and $V_{\text{mid}3}$ can be calculated from the “OFF-to-ON transition” and “ON-to-OFF transition” processes.

In the OFF-to-ON transition, V_{pv} drops from $V_{\text{mid}1}$ to $V_{\text{mid}2}$ during $T_{\text{off,on}}$ and we have

$$V_{\text{mid}2} = V_{\text{mid}1} - \int_0^{T_{\text{off,on}}} \frac{I_{\text{ctrl}} + I_{\text{off,on}} - I_{\text{pv}}}{C_{\text{bulk}} + C_{\text{decoup}}} dt, \quad (18)$$

where $V_{\text{mid}1}$ can be obtained from (14).

In the ON-to-OFF transition, V_{pv} drops from $V_{\text{mid}3}$ to V_l during $T_{\text{on,off}}$ and we have:

$$V_{\text{mid}3} = V_l + \int_0^{T_{\text{on,off}}} \frac{I_{\text{ctrl}} + I_{\text{on,off}} - I_{\text{pv}}}{C_{\text{bulk}} + C_{\text{decoup}}} dt. \quad (19)$$

Therefore, we can express T_{task} by substituting (18) and (19) into (17). T_{on} is obtained by substituting (17) and (16) into (13).

3) *Expression of system efficiency:* Finally, we obtain the expression of the system efficiency in (20) by merging (10), (13) and (17) into (1). All parameters can be extracted from the component models directly.

Noted that (20) holds when I_{pv} meets the constraints in (9) and (12), we combine them in the following:

$$I_{\text{ctrl}} < I_{\text{pv}} < I_{\text{ctrl}} + \min\{I_{\text{on,off}}, I_{\text{off,on}}, I_{\text{task}}\}. \quad (21)$$

B. Discussion

Although the system efficiency is defined in (1) and calculated by (20), they cannot explicitly show how η_{sys} is affected by the design parameters. To make further analysis, we rewrite (1) and factorize η_{sys} to two factors. One is the MPPT efficiency indicating the MPP tracking performance of the PV module. The other is the transfer efficiency, which denotes the proportion of harvested energy to execute the workload. The factorization is shown in (22).

$$\begin{aligned} \eta_{\text{sys}} &= \frac{P_{\text{task}} T_{\text{task}}}{P_{\text{mpp}} T_{\text{dpm}}} \\ &= \underbrace{\frac{P_{\text{pv,avg}}}{P_{\text{mpp}}}}_{\eta_{\text{MPPT}}} \times \underbrace{\frac{P_{\text{task}} T_{\text{task}}}{P_{\text{pv,avg}} T_{\text{dpm}}}}_{\eta_{\text{trans}}}. \end{aligned} \quad (22)$$

Thus, the system efficiency can be optimized from two aspects: the MPPT tracking and the energy transferring. We discuss them separately in the following paragraphs.

1) *MPPT efficiency:* In the proposed PV system, V_{pv} swings in a small range $[V_l, V_h]$. We call it *MPPT window* and its width is denoted as $\Delta V = (V_h - V_l)$. The MPPT efficiency depends on the MPPT window, because the output power is determined by the operating voltage of the PV module. According to the P-V curve in Fig. 5(b), the MPPT efficiency is expressed as follows:

$$\eta_{\text{MPPT}} = \frac{P_{\text{pv,avr}}}{P_{\text{mpp}}} = \frac{\int_{V_l}^{V_h} p(v) dv}{P_{\text{mpp}} \Delta V}, \quad (23)$$

where $p(v)$ is extracted from the P-V curve, and $p_{\text{pv,avr}}$ is the average power in the MPPT window.

Fig. 8 is drawn to better understand how the MPPT window affects η_{MPPT} . η_{MPPT} in (23) can be considered as a fill factor to present the ratio of the red shaded area to fill the red rectangle in Fig. 8(a). We fix the ΔV and move the MPPT window. We have the following theorem:

Theorem 1: If the MPPT window width ΔV is a constant, the maximum η_{MPPT} can be achieved when and only when $p(v_l) = p(v_h)$.

To prove this theorem, we assume that an initial MPPT window satisfies $p(v_l) = p(v_h)$. If we move the MPPT window right by δV (see in Fig. 8(a)), the area of unfilled part will subtract ΔS_1 and add ΔS_2 . Because $p(v)$ is convex around MPP, ΔS_1 is larger than ΔS_2 . Therefore, the fill factor of the initial MPPT window is larger than the moved one. Similar conclusion holds when the MPPT window moves left by δV . Consequently, Theorem 1 is proved.

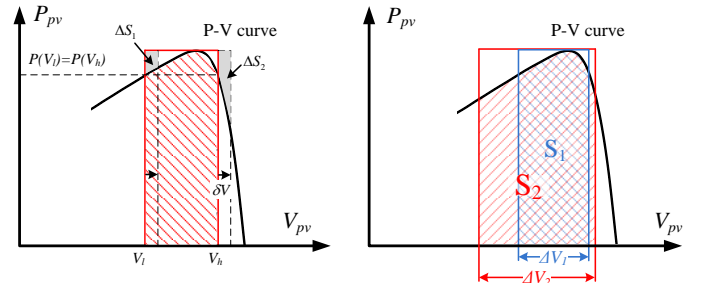


Fig. 8. (a) Varying the position of MPPT window with a fixed MPPT window width. (b) Varying the width of MPPT window when guaranteeing $p(V_l) = p(V_h)$.

On the other hand, we vary ΔV while keeping $p(V_l) = p(V_h)$. As Fig. 8(b) has shown, it is obviously that $\frac{S_1}{\Delta V_1} > \frac{S_2}{\Delta V_2}$. That means a smaller ΔV results in a higher fill factor, hence a higher η_{MPPT} . The maximal η_{MPPT} can be achieved as follows

when $p(V_l) = p(V_h)$ and $\Delta V \rightarrow 0$:

$$\lim_{\Delta V \rightarrow 0} \eta_{MPPT} = \lim_{\Delta V \rightarrow 0} \frac{\int p(v)dv}{P_{mpp}\Delta V} = 100\%. \quad (24)$$

2) *Transfer efficiency*: The transfer efficiency can be expressed as follows:

$$\eta_{trans} = \frac{P_{task}T_{task}}{P_{pv,avg}T_{dpm}} = \frac{P_{task}(T_{ON} - T_{other})}{P_{pv,avg}T_{dpm}}, \quad (25)$$

where $T_{other} = T_{cs} + T_{on,off} + T_{off,on}$. If we shrink ΔV , both T_{ON} and T_{dpm} decrease. Therefore, it is hard to say whether η_{trans} increases or decreases. If we consider an extreme condition that T_{ON} is reduced to T_{other} , both T_{task} and η_{trans} are zero. It implies that we can not reduce ΔV unlimitedly, otherwise there is no time for task execution and η_{trans} becomes zero.

If we jointly consider η_{MPPT} and η_{trans} , the reduction of ΔV can improve η_{MPPT} but possibly degrade η_{trans} . Therefore, it is necessary to choose a proper ΔV in order to maximize the system efficiency. We will discuss the optimization method of MPPT window in Section V.

V. SYSTEM OPTIMIZATION

This section discusses optimizing techniques to maximize the system efficiency. The design knobs include two categories. The first one consists of design-time parameters, such as PV module, bulk and decoupling capacitors. The second one contains the run-time parameters, such as the MPPT window which is tunable during the operation.

A. Design-time Optimization

1) *PV module Sizing*: Stacked in parallel, the PV cells will increase the output current of the PV module, while keeping the MPP voltage constant. According to the models in Section III, we evaluate the efficiency of system, MPPT module and transfer under different sizes of PV module in Fig. 9.

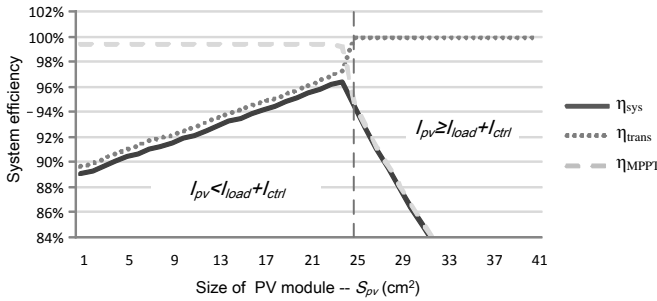


Fig. 9. Effects of the PV module size on system efficiency, MPPT efficiency and transfer efficiency. ($C_{bulk} = 47 \mu F$, $C_{decoup} = 20 nF$, $[V_l, V_h] = [2.70 V, 2.90 V]$, Solar irradiation = $300 W/M^2$).

In Fig. 9, the system efficiency increases when a larger PV module is used. It is because a larger I_{pv} reduces T_{OFF} but increases T_{task} (according to (10) and (17)), which boosts the system efficiency η_{sys} . However, it decreases after the size of PV module S_{pv} is larger than a threshold (In this case, the threshold is $25 cm^2$). Because I_{pv} exceeds the constraint

in (21), it is clamped to the load current and fails to track the MPP. Though the transfer efficiency is nearly 100%, the MPPT efficiency falls rapidly, which leads to a lower η_{sys} . In a word, a larger PV module leads to a higher system efficiency, as long as it meets the constraints in (21).

2) *Capacitors Sizing*: We size the bulk and decoupling capacitors to optimize the system efficiency, since they jointly determine the energy loss during the transitions (“ON-to-OFF transition” and “OFF-to-ON transition”), and during the charge sharing process. According to Fig 3, the transition energy loss $E_{tran,loss}$ comes from two voltage drops in each DPM cycle and it is expressed as below:

$$E_{tran,loss} = \frac{1}{2}(C_{bulk} + C_{decoup})(V_{mid1}^2 - V_{mid2}^2 + V_{mid3}^2 - V_l^2). \quad (26)$$

Thus, the system efficiency loss caused by transitions is expressed as:

$$\Delta\eta_{sys,1} = \frac{E_{tran,loss}}{E_{mpp}} = \frac{P_{tran,loss}T_{dpm}}{P_{mpp}T_{dpm}} = \frac{P_{tran,loss}}{P_{mpp}}. \quad (27)$$

The charge sharing energy loss is caused due to the voltage drop at the beginning of the DPM cycle, which is calculated as below:

$$E_{share,loss} = \frac{1}{2}C_{bulk}V_h^2 - \frac{1}{2}(C_{bulk} + C_{decoup})V_{mid1}^2. \quad (28)$$

The system efficiency loss caused by charge sharing is expressed as:

$$\Delta\eta_{sys,2} = \frac{E_{share,loss}}{E_{mpp}}. \quad (29)$$

Based on the equations above, we evaluate $\Delta\eta_{sys,1}$ and $\Delta\eta_{sys,2}$ under different C_{bulk} and C_{decoup} . In Fig. 10 (a), we can see

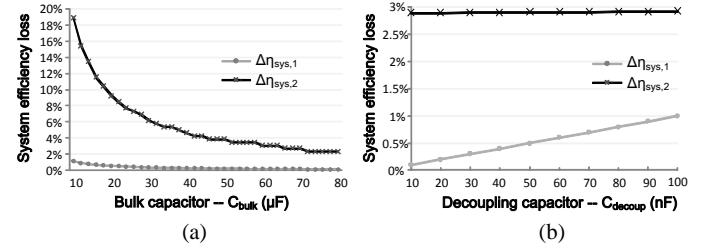


Fig. 10. System efficiency loss caused by transition loss ($\Delta\eta_{sys,1}$) and charge sharing loss ($\Delta\eta_{sys,2}$) under different C_{bulk} and C_{decoup} . ($S_{pv} = 15 cm^2$, Solar irradiation = $250 W/M^2$, $[V_l, V_h] = [2.68 V, 2.88 V]$).

that a larger C_{bulk} always leads to smaller energy loss in both transition and charge sharing processes. It is because a larger C_{bulk} prolongs T_{task} and T_{dpm} , which reduces the DPM times as well as the total energy loss. However, this conclusion only holds in a certain range. If the capacitor becomes large enough (several farads), the leakage and charging efficiency will dominate the energy loss.

On the other hand, a larger C_{decoup} degrades the system efficiency in Fig. 10 (b) due to more charge sharing. It has a little impact on the system efficiency, because $C_{decoup} \ll C_{bulk}$. However, the decoupling capacitor is used to maintain the power integrity of electronic load. Its size cannot be too small to keep the power noise under the system tolerance. The minimal value is related to the operating voltage, peak current,

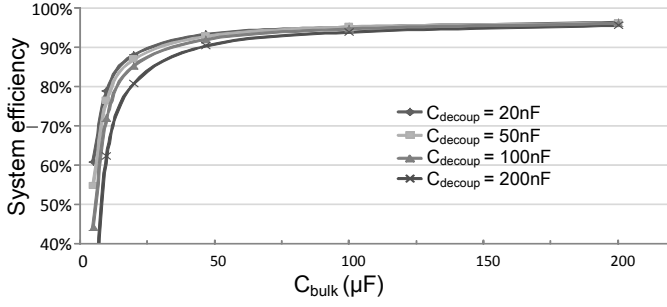


Fig. 11. System efficiency under different C_{bulk} and C_{decoup} . ($S_{pv} = 15 \text{ cm}^2$, Solar irradiation= 250 W/m^2 , $[V_l, V_h] = [2.68 \text{ V}, 2.88 \text{ V}]$).

and impedance of the load. In the prototype from Section VI, the minimal C_{decoup} is 20 nF . In a word, we should take the minimal C_{decoup} to guarantee the power integrity as well as high system efficiency.

Finally, we jointly evaluate the system efficiency under different combinations of C_{bulk} and C_{decoup} in Fig. 11. The system efficiency rises when C_{bulk} increases or C_{decoup} shrinks. Furthermore, we can see that the improvement of system efficiency is not significant when C_{bulk} is larger than a threshold (50 μF). When C_{bulk} is larger than 100 μF , the system efficiency of the prototype is about 95%. However, it requires 2-3 times larger C_{bulk} to achieve 1% gain of the system efficiency. As a large C_{bulk} suffers from high leakage, large size and costs, it is not reasonable to increase C_{bulk} unlimitedly.

B. Run-time optimization

Section IV-B shows that the system efficiency is related to the position and width of MPPT window. Fig. 12 illustrates the system efficiency under different settings of V_l and V_h . The system efficiency locates on a convex surface with the maximum value of 93.5%, when $[V_l, V_h]$ equals to $[2.56 \text{ V}, 2.94 \text{ V}]$. This figure demonstrates that an optimal MPPT window exists to maximize the system efficiency. Therefore, a run-time optimizing algorithm should be developed to find out the optimal MPPT window.

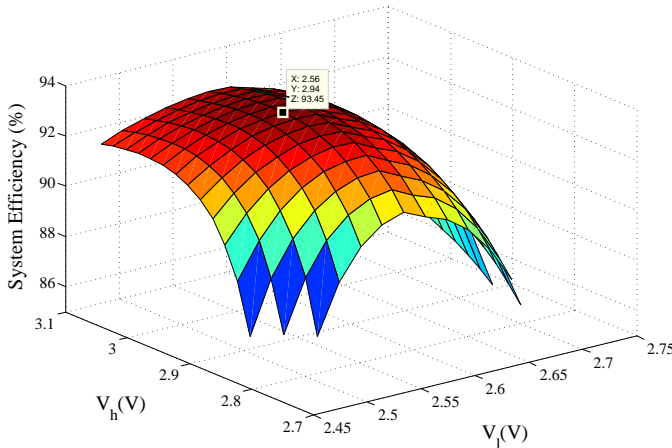


Fig. 12. System efficiency under different MPPT window settings ($S_{pv} = 15 \text{ cm}^2$, Solar irradiation= 200 W/M^2 , $C_{bulk} = 47 \text{ μF}$, $C_{decoup} = 20 \text{ nF}$).

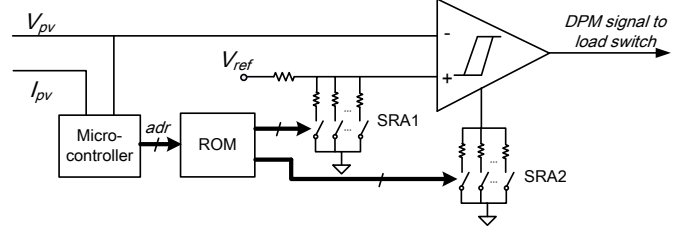


Fig. 13. The hardware design of the MPPT controller for on-line MPPT window tuning.

Once the I-V characteristic is given, the MPPT controller can find the optimal window by searching the maximum point on the convex surface. However, it is power and time consuming to implement a complex algorithm on the sensor nodes. Moreover, the I-V characteristic of a PV module varies with the solar irradiance. A complex MPPT window tuning on a power efficient platform cannot catch up with the real time irradiance variation. Therefore, we propose a hybrid offline-online MPPT window tuning method. In the offline stage, we determine a reference set of solar irradiance, $\{S_i\} = \{S_1, S_2, \dots, S_n\}$, and calculate the reference set of I-V characteristics, $\{I_i(V)\}$, from $\{S_i\}$. The set of optimal MPPT windows, $\{W_i\}$, are given out and stored in a ROM. In the online tuning stage, the MPPT controller samples V_{pv} and I_{pv} of the PV module, and chooses the closest point:

$$index = \arg \min_i |I_i(V_{pv}) - I_{pv}|, \quad (30)$$

The MPPT controller selects the corresponding W_{index} from the ROM as the optimal MPPT window.

The hardware design of the proposed MPPT window tuning is shown in Fig. 13. The tuning of MPPT window is realized by two switched-resistors arrays (SRA1 and SRA2) attached to a adjustable hysteresis comparator. The resistance of SRAs can be configured by changing the on/off state of the switches. In the proposed design, the SRA1 tunes the MPPT window upper bound V_h and SRA2 tunes the MPPT window width ΔV . The MPPT window is set as $[V_h - \Delta V, V_h]$. The ROM stores the $\{W_i\}$ in terms of SRAs' configurations. The microcontroller samples V_{pv} and I_{pv} with an analog-to-digital converter and selects the best SRAs' configurations from the ROM.

In the proposed MPPT window tuning method, the online operation includes sampling V_{pv} and I_{pv} , and comparing it with each $I_i(V)$ in a lookup table. Since we only store the values around the MPP, the lookup table does not occupy lots of memory space. (For a set of 10 I-V characteristics with 0.01 V resolution, the memory occupation is around 1KB). All of those operations can be easily realized by a trivial customized circuit, which is out of the scope of this paper. Although the proposed method is an approximated approach, we evaluate the tuning speed and related error of the algorithm in Section VII-C, which is qualified for the real prototype.

VI. VALIDATION

Before exploring the proposed PV system by the simulator based on the component models, we implemented a corresponding nonvolatile prototype. In addition to demonstrating the working mechanism and high efficiency of the proposed

system,, it enables us to gain insights to the accuracy of the simulator.

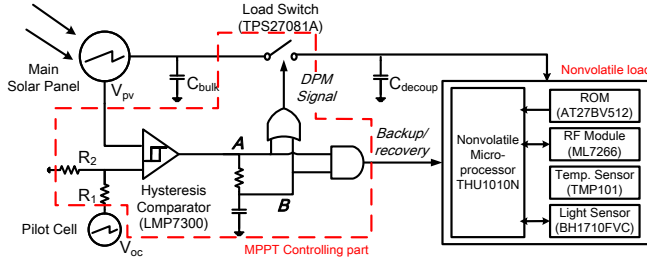


Fig. 14. Block diagram of the evaluation prototype.

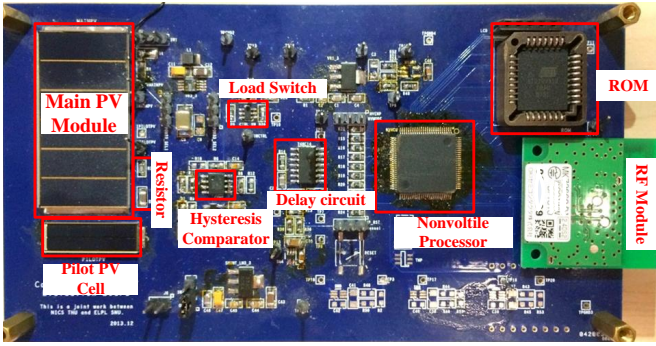


Fig. 15. Photograph of the PCB of the prototype.

A. Prototype description

The block diagram of the prototype is shown in Fig. 14. We use the fractional open-circuit voltage (FVoc) technique [7] to implement the MPPT. The MPP voltage of a PV module can be approximated as $V_{mpp} = K_{foc}V_{oc}$, where V_{oc} represents the open-circuit voltage. A pilot cell, with the same voltage characteristic as the main solar panel, is used to provide V_{oc} and K_{foc} is set as $R_2/(R_1 + R_2)$.

The MPPT controlling part includes the resistors, the load switch, the delay circuit, the logic gates and the hysteresis comparator. The hysteresis comparator compares the fractional V_{oc} with the output voltage V_{pv} to clamp it around V_{mpp} . It is connected to an RC delay unit and two logic gates, in order to generate the DPM and backup/recovery signals. The modules in the MPPT controlling part are shown in Table IV. Fig. 15 shows their locations on board. The MPPT controlling part only consumes $140 \mu W$ in total, which is much smaller than the nonvolatile load.

The nonvolatile load consists of a nonvolatile microprocessor, a ROM as the instruction memory, a low power RF transceiver, and two sensors. Their specifications are shown in Table V, and Fig. V shows their locations on board. We use a Data Acquisition Card (DAQ) [26] to capture the voltage and current of each module via test pins. In the following, we compare the results simulation and measurements to validate the DPM working mechanism and modeling accuracy.

TABLE IV
SPECIFICATION OF COMPONENTS IN THE MPPT CONTROLLING PART.

Component	Part No.	Value	Power consumption
Load Switch	TPS27081	-	$30 \mu W$
Hysteresis comparator	LMP7300	-	$50 \mu W$
Delay circuit	74HC14	-	$6 \mu W$
OR gates	74AHC1G08	-	$2 \mu W$
AND gate	74AHC1G32	-	$3 \mu W$
Resistor	R1/R2	$20k \Omega / 200k \Omega$	$50 \mu W$

TABLE V
SPECIFICATION OF COMPONENTS IN THE NONVOLATILE LOAD.

Component	Part No.	Active Power	$I_{off,on}$	$I_{on,off}$	$T_{off,on}$	$T_{on,off}$
MCU	THU1010N	3.29 mW	2.2 mA	1.8 mA	3 μs	7 μs
ROM	AT27LV010A	16.5 mW	4.8 mA	0	2 μs	0
RF Transceiver	ML7266	16.24 mW	1.7 mA	0	41 μs	0
Temp. Sensor	TMP101	3.1 mW	1.0 mA	0	5 μs	0
Light Sensor	BH1710FVC	1.24 mW	0.1 mA	0	5 μs	0

B. DPM working mechanism

To validate the DPM working mechanism, we capture the waveform of V_{pv} and the DPM signal using the oscilloscope. We compare it with the simulated results under the same experimental setup, where $Solar\ irradiation = 200 W/m^2$, $S_{pv} = 15 cm^2$, $C_{bulk} = 47 \mu F$ and $C_{decoup} = 20 nF$. In Fig. 16, the red line represents the simulated waveform and the grey line represents the measured waveform.

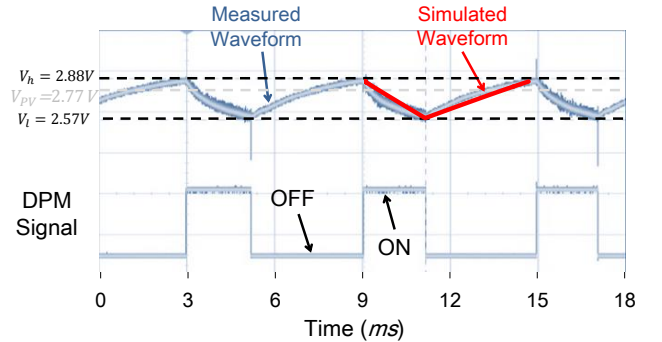


Fig. 16. Waveforms of the PV module output voltage and DPM signal on prototype measurement and simulation.

As we can see, the DPM period T_{dpm} of the simulated waveform is a little shorter than the measured one and the maximum error is within 6%. It is because the prototype has some non-ideal factors, such as the variations of capacitor and solar panel size and parasitic leakage paths that slow down the capacitor charging. The maximum observed difference of V_{pv} during a DPM cycle between two waveforms is 3%. Therefore, we can conclude that the simulated waveforms can reflect the actual DPM working mechanism of the prototype under acceptable accuracy.

C. Energy efficiency

Furthermore, we evaluate the accuracy of the energy efficiency under different solar irradiance. The prototype board

TABLE VI
SYSTEM EFFICIENCY ON PROTOTYPE MEASUREMENT AND SIMULATION
UNDER DIFFERENT SOLAR IRRADIANCE.

Solar Irradiance (W/m^2)	System Efficiency		Error (%)	V_{mpp} (V)	MPPT Window (V)
	Measured	Simulation			
100	84.32%	92.50%	8.2%	2.70	[2.48 2.83]
120	86.27%	92.56%	6.3%	2.72	[2.49 2.84]
140	88.10%	93.05%	5.9%	2.73	[2.52 2.85]
160	88.89%	93.11%	4.2%	2.75	[2.54 2.87]
180	89.45%	93.18%	3.7%	2.76	[2.55 2.90]
200	90.25%	93.5%	3.3%	2.77	[2.57,2.94]
250	90.47%	93.9%	3.0%	2.81	[2.61,2.99]
300	91.80%	94.4%	2.6%	2.86	[2.64,3.04]
350	92.02%	94.8%	2.8%	2.89	[2.67,3.08]
400	92.15%	94.9%	2.7%	2.92	[2.71,3.10]
440	90.87%	94.8%	4.1%	2.93	[2.73,3.12]

consists of a main solar panel and several capacitors, which are valued as: $S_{pv} = 15 \text{ cm}^2$, $C_{bulk} = 47 \text{ }\mu\text{F}$, $C_{decoup} = 20 \text{ nF}$. According to $\frac{E_{task}}{E_{mpp}}$, the energy efficiency is measured as follows. First, a quasi-static scanning is used to explore the I-V characteristics of the main solar cell, where V_{mpp} and P_{mpp} can be extracted. After that, the hysteresis window of the comparator is tuned to the optimal MPPT window. The P_{task} of an electronic load is sampled under a 250 KHz rate. Finally, we calculate E_{task} as the integral of P_{task} on T_{task} and E_{mpp} is the product of P_{mpp} and T_{task} .

The following setups are used in the simulations: i, adjust the parameters of the PV module to have the same I-V characteristics as the main solar panel; ii, set the same MPPT window as the prototype; iii, set the same average load power consumption as the measured P_{task} . The energy efficiency can be simulated according to (20). The comparison results between measurement and simulation are given in Table VI.

In Table VI, when the solar irradiance increases from 100 W/m^2 to 440 W/m^2 ¹, the difference between the measurements and the simulation decreases to 3.0%. It is because that the non-ideal factors, such as leakages, are more significant, when the lower solar irradiance causes longer time to charge the bulk capacitor. When the solar irradiance is above 400 W/m^2 , the solar output current does not match $I_{pv} < I_{ctrl} + I_{load}$ in (11). The MPP tracking is failed, and the system efficiency decreases. However, the total energy efficiency is still high (84% – 92%) in the wide range of solar irradiance, and the simulation matches well with the measurements.

Based on all comparisons between the simulation and measurement on the real prototype, it is clear that the given simulation models accurately describe the system functions and calculate the overall energy efficiency. We will use the validated models as well as the prototype to further evaluate the proposed PV system in the next section.

VII. SYSTEM EVALUATION

In this section, we evaluate different system metrics by both simulations and measurements. First, we illustrate the

experimental setups and define two baselines for comparisons. After that, energy efficiency is compared among three systems by simulations with breakdown of energy loss. We validate the performance of MPPT tuning method in Section VII-C. Finally, the effectiveness of the proposed architecture is measured by comparing the converter-less prototype with a conventional system.

A. Experimental Setup

We build two baseline systems to evaluate advantages of the proposed system, coming from the nonvolatile microprocessor and the converter-less MPPT architecture. The first system is the *volatile microprocessor baseline*. It replaces the nonvolatile microprocessor in the proposed system with a volatile one [27], whose backup and recovery time are $300 \text{ }\mu\text{s}$ and $200 \text{ }\mu\text{s}$. The second system is the *conventional MPPT baseline*, which includes two cascaded converters and a supercapacitor [28].

Constant voltage principle is used in the MPP tracking of the proposed system and the volatile microprocessor baseline. The voltage window $[V_l, V_h]$ is $[2.75 \text{ V}, 2.90 \text{ V}]$. The bulk capacitor and decoupling capacitor are $47 \text{ }\mu\text{F}$ and 20 nF . In the conventional MPPT baseline, the supercapacitor is 0.2 F and two cascaded converters use the parameters in [28].

All three systems are powered by the same PV module and run the same workloads. The PV module size is 15 cm^2 and its MPP voltage is 3 V . By minimizing the PV module size, the system works under a DPM manner during the whole day. Other parameters are summarized in Table I.

B. System Efficiency

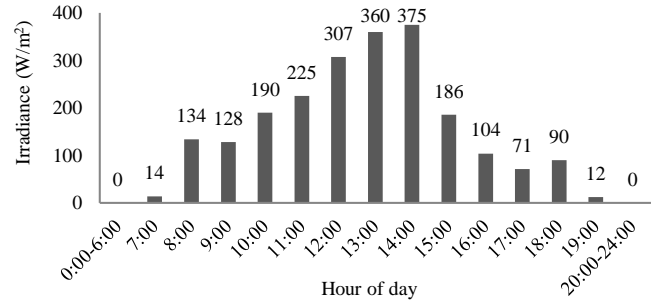


Fig. 17. Hourly solar irradiance during a day.

First, we compare the energy efficiency of three systems in a day. Fig. 17 shows the hourly solar radiation data in a cloudy day from National Solar Radiation Data Base [29]. The solar irradiance equals to the average value during the last one hour². Given the data in Fig. 17, we compare the overall energy efficiency of each system as below.

Fig. 18 shows the breakdown of the energy consumption of each system according to the validated models (Section VI). The effective energy is the energy for task execution, while the remaining parts are energy loss. Fig. 18(a) shows the breakdown of the conventional MPPT baseline. Its energy

¹It is a typical solar irradiance in normal outdoor conditions

²The average solar irradiance is used to simplify the simulation, but the proposed method is not restricted to the assumption.

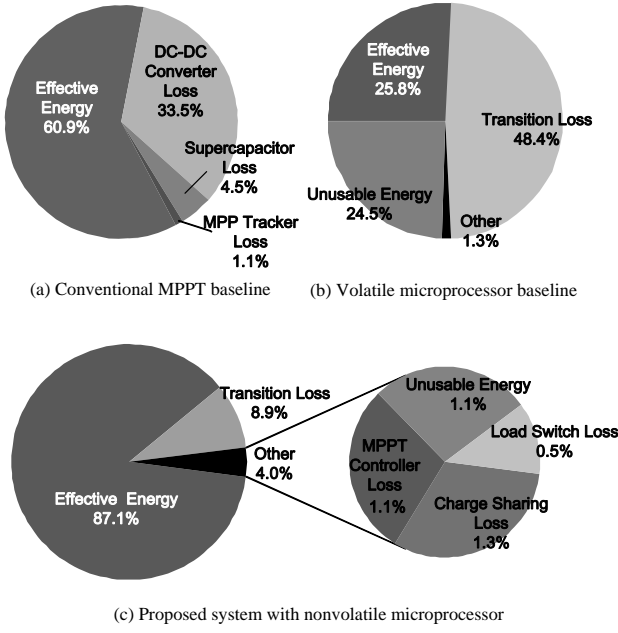


Fig. 18. Energy breakdown pie graphs of the three different PV power systems.

loss mainly comes from the converters and the supercapacitor. They contribute 37.3% energy to the total system. Its overall energy efficiency is 60.9%. The volatile microprocessor baseline avoids those energy loss by removing the converters and the supercapacitor. However, as Fig. 18(b) shows, the large transition overheads of the volatile microprocessor contribute 48.4% energy loss. Moreover, this system can not work under weak solar radiation (see in Table VI), which leads to 24.5% solar energy wasted as “unusable energy”. Those factors render its system efficiency even worse than the conventional MPPT baseline. Observing those challenges, we adopt the nonvolatile microprocessor to improve the transition performance. As Fig. 18(c) shows, the transition loss is reduced to 8.9%. Other components, such as charge sharing, MPPT controller, load switch and unusable energy, contribute extra 4% energy loss in all. The overall energy efficiency is 87.1%, which is much better than above two baselines. In sum, the proposed system has the least energy loss among the three systems, thanks to its small transition overheads and the storage-less and converter-less architecture.

To compare the continuous performance of those systems, we set up Table VII to show the performances of the proposed system and the volatile microprocessor baseline during a day. D_{dpm} is the duty ratio of a cycle, which is $\frac{T_{task}}{T_{dpm}}$. E_{mpp} and E_{task} represent the energy of the MPPT output and task execution, where η_{sys} is $\frac{E_{task}}{E_{mpp}}$. Column 4 and 8 indicate whether the system can work at the corresponding time slots. The proposed system works during 8 : 00 ~ 18 : 00, while the baseline only works during 10 : 00 ~ 15 : 00. It implies that the proposed system can operate even under weak solar irradiance. The system efficiency of the proposed system in Column 7 reaches 87.1% in average and 92.8% in maximum. However, the corresponding energy efficiency of the volatile microprocessor baseline in Column 11 only reaches 25.8% and 54.4%. Furthermore, the overall D_{dpm} of the proposed

TABLE VII
SYSTEM EFFICIENCY AND DPM DUTY RATIO DURING A DAY.

Common statistics			Proposed System				Volatile Microprocessor Baseline			
Time	V_{mpp} (V)	E_{mpp} (J)	Work	E_{task} (J)	D_{dpm} (%)	η_{sys} (%)	Work	E_{task} (J)	D_{dpm} (%)	η_{sys} (%)
7:00	2.52	2.9	No	0	0	0	No	0	0	0
8:00	2.73	30.4	Yes	25.3	20.3	83.3	No	0	0	0
9:00	2.72	29.0	Yes	24.1	19.3	83.0	No	0	0	0
10:00	2.76	43.6	Yes	37.8	30.3	86.5	Yes	2.8	2.2	6.4
11:00	2.78	51.9	Yes	45.7	36.7	87.9	Yes	8.1	6.4	15.5
12:00	2.81	71.6	Yes	65.2	52.4	91.0	Yes	26.6	21.3	37.1
13:00	2.82	84.4	Yes	78.1	62.7	92.5	Yes	42.9	34.4	50.9
14:00	2.82	88.0	Yes	81.7	65.7	92.8	Yes	47.9	38.4	54.4
15:00	2.76	42.7	Yes	36.9	29.6	86.4	Yes	2.5	2.0	5.8
16:00	2.71	23.4	Yes	18.7	15.0	80.0	No	0	0	0
17:00	2.67	15.7	Yes	11.7	9.4	74.4	No	0	0	0
18:00	2.69	20.1	Yes	15.8	12.7	78.4	No	0	0	0
19:00	2.50	2.5	No	N/A	0	0	No	0	0	0
Overall		506.3		440.9	27.3	87.1		130.7	8.1	25.8

system in Column 6 is 27.3%, 3.4X larger than that (8.1%) in Column 10. It implies that the proposed system executes more tasks during a day than the volatile microprocessor baseline. It is because the proposed system has much smaller transition overheads, resulting in more time and energy for task execution.

C. Performance of MPPT window tuning

Section V-B presents a hybrid offline-online MPPT window tuning method to operate the proposed PV system efficiently. We evaluate its effectiveness as follows. Both MPPT window tuning accuracy and speed are considered. To evaluate the accuracy, we compare both MPPT window and system efficiency from the proposed method with optimal values. To evaluate the speed, we compare the tuning time between the proposed algorithm and a brute-force searching one. Both algorithms are running on a MSP430 microcontroller.

Table VIII shows the experimental results. Column 2 and 3 compare the obtained tuning windows with the optimal ones. The average error is 0.2%. Column 4 and 5 give the system efficiency under the corresponding MPPT windows. The average error is 0.04%. They indicate that the accuracy of the proposed MPPT window tuning method is reasonable. Column 6 and 7 compare the speed of the MPPT window tuning. In general, the proposed method completes within seconds to follow the environmental changes. By contrast, the brute-force searching one consumes thousands of seconds, i.e. tens of minutes, to complete the tuning. It is too slow to follow the solar variations. Above results demonstrate that the proposed hybrid offline-online MPPT window tuning method satisfies the tuning speed with reasonable accuracy loss.

D. Prototype measurement

To sum all factors together, we constructed both prototypes for proposed PV system and *conventional MPPT baseline*. We compare their energy efficiency by measurements. In the conventional MPPT prototype, we use the solar panel to charge the supercapacitor from 1.5 V to 3.0 V, and discharge it to 1.5 V by driving workloads. We set the same working period in the proposed PV system. We measure data under

TABLE VIII
PERFORMANCE OF THE PROPOSED HYBRID OFFLINE-ONLINE MPPT
WINDOW TUNING METHOD.

Condition	$[V_{l,opt}, V_{h,opt}]$		η_{sys}		Tuning Speed	
Solar Irra.	Proposed Method	Optimal	Proposed Method	Optimal	Proposed Method	Total Online
(W/m^2)	(V)	(V)	(%)	(%)	(s)	(s)
110	[2.479, 2.830]	[2.483, 2.834]	92.52	92.53	1.7	1464
130	[2.493, 2.842]	[2.503, 2.848]	92.58	92.60	2.1	1487
150	[2.524, 2.859]	[2.532, 2.863]	93.08	93.09	2.4	1379
170	[2.539, 2.870]	[2.544, 2.874]	93.12	93.14	2.8	1428
190	[2.569, 2.884]	[2.563, 2.881]	93.22	93.42	3.1	1451
210	[2.569, 2.884]	[2.575, 2.889]	93.47	93.49	3.2	1432
Summary	Avg. Error 0.2%		Avg. Error 0.04%		Acceleration 448 – 861X	

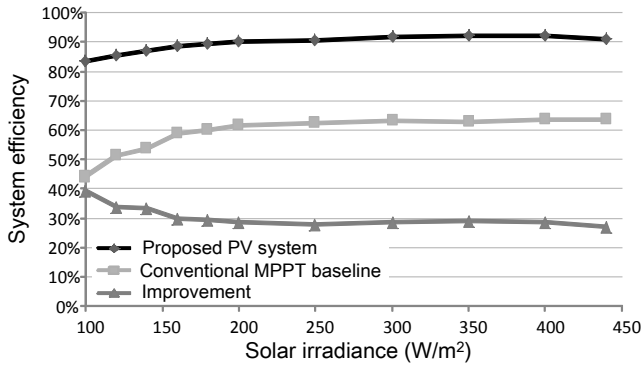


Fig. 19. System efficiency measurements on the proposed PV system and conventional MPPT baseline.

different solar irradiance conditions ranging from $100 W/m^2$ to $450 W/m^2$.

Fig. 19 illustrates that the system efficiency increases with a larger solar irradiance in both systems. The proposed PV system reaches an energy efficiency ranging from 84% to 92%. The energy efficiency of the conventional MPPT prototype ranges from 44% to 61%. The energy efficiency improvements range from 27% to 39%. The average improvement is 30.6%. When the irradiance is under $200 W/m^2$, the improvement decreases with the larger solar irradiance. It implies that the conventional MPPT baseline gains more from the larger solar power. When the irradiance is above $250 W/m^2$, the system efficiency of both prototypes improves slowly, because the energy loss cannot be reduced by increasing the solar irradiance. When the irradiance is larger than $400 W/m^2$, the proposed PV system does not match $I_{pv} < I_{ctrl} + I_{load}$, and the system efficiency decreases.

VIII. CONCLUSION

This paper introduces a breakthrough idea for maintenance-free, low-cost and high efficiency photovoltaic energy harvesting system. The proposed idea is a radical change of conventional design concept: use of the maximum power point tracking charger, a supercapacitor, and a voltage regulator. These components are root causes of high energy loss, short lifetime, large volume, etc. We eliminate the DC-DC converters and directly connect the PV cell to the nonvolatile microprocessor. We perform MPPT through a very fine-grain dynamic power management of the nonvolatile microprocessor in a

few hundred microseconds. The system efficiency significantly benefits. We achieve an overall system efficiency of 87.1% during a whole day, and the proposed system is operational even under a very weak solar irradiance. **The proposed idea is not limited to IoT applications though it has been validated with an IoT sensor platform. It is applicable to any low-power applications with photovoltaic energy harvesting and saves cost and form factors.**

REFERENCES

- [1] J. Bryzek, "Roadmap for the trillion sensor universe," 2013.
- [2] Y. Zhang, F. Zhang, Y. Shakhsheer, J. D. Silver, A. Klinefelter, M. Nagaraju, J. Boley, J. Pandey, A. Shrivastava, E. J. Carlson *et al.*, "A batteryless 19 w mics/ism-band energy harvesting body sensor node soc for exg applications," *IEEE Journal of Solid-State Circuit*, 2013.
- [3] M. Sun, L. E. Burke, Z.-H. Mao, Y. Chen, H.-C. Chen, Y. Bai, Y. Li, C. Li, and W. Jia, "ebutton: A wearable computer for health monitoring and personal assistance," in *DAC*, 2014.
- [4] M. Raju and M. Grazier, "Energy harvesting. ulp meets energy harvesting: a game-changing combination for design engineers," *TI*, <http://focus.ti.com/lit/wp/slyy018/slyy018.pdf>, 2008.
- [5] D. Brunelli, L. Benini, C. Moser, and L. Thiele, "An efficient solar energy harvester for wireless sensor nodes," in *DATE*, 2008.
- [6] D. Brunelli, C. Moser, L. Thiele, and L. Benini, "Design of a solar-harvesting circuit for batteryless embedded systems," *IEEE Trans. on Circuits and Systems I: Regular Papers*, 2009.
- [7] D.-Y. Lee, H.-J. Noh, D.-S. Hyun, and I. Choy, "An improved mppt converter using current compensation method for small scaled pv-applications," in *APEC*, 2003.
- [8] V. V. Scarpa, S. Buso, and G. Spiazzi, "Low-complexity mppt technique exploiting the pv module mpp locus characterization," *IEEE Trans. on Industrial Electronics*, 2009.
- [9] X. Li, U. Dennis Heo, K. Ma, V. Narayanan, H. Liu, and S. Datta, "Rf-powered systems using steep slope devices," in *NEWCAS*, 2014.
- [10] H. Liu, X. Li, R. Vaddi, K. Ma, S. Datta, and V. Narayanan, "Tunnel fet rf rectifier design for energy harvesting applications," *IEEE Journal on Emerging and Selected Topics in Circuits and Systems*, 2014.
- [11] B. Sahu and G. A. Rincon-Mora, "An accurate, low-voltage, cmos switching power supply with adaptive on-time pulse-frequency modulation (pfm) control," *IEEE Trans. on Circuits and Systems I: Regular Papers*.
- [12] Q. Xie, Y. Wang, Y. Kim, M. Pedram, and N. Chang, "Charge allocation in hybrid electrical energy storage systems," *IEEE Trans. on Computer-Aided Design of Integrated Circuits and Systems*, 2013.
- [13] F. I. Simjee and P. H. Chou, "Efficient charging of supercapacitors for extended lifetime of wireless sensor nodes," *IEEE Trans. on Power Electronics*, 2008.
- [14] F. Simjee and P. H. Chou, "Everlast: long-life, supercapacitor-operated wireless sensor node," in *ISLPED*, 2006.
- [15] Y. Choi, N. Chang, and T. Kim, "Dc-dc converter-aware power management for low-power embedded systems," *IEEE Trans. on Computer-Aided Design of Integrated Circuits and Systems*, 2007.
- [16] S. Kim and P. H. Chou, "Size and topology optimization for supercapacitor-based sub-watt energy harvesters," *IEEE Trans. on Power Electronics*, 2013.
- [17] A. S. Weddell, G. V. Merrett, T. J. Kazmierski, and B. M. Al-Hashimi, "Accurate supercapacitor modeling for energy harvesting wireless sensor nodes," *IEEE Trans. on Circuits and Systems II: Express Briefs*, 2011.
- [18] S. Liu, J. Lu, Q. Wu, and Q. Qiu, "Load-matching adaptive task scheduling for energy efficiency in energy harvesting real-time embedded systems," in *ISLPED*, 2010.

- [19] S. Liu, Q. Wu, and Q. Qiu, "An adaptive scheduling and voltage/frequency selection algorithm for real-time energy harvesting systems," in *DAC*, 2009.
- [20] D. Brunelli and L. Benini, "Designing and managing sub-milliwatt energy harvesting nodes: opportunities and challenges," in *VITAE*, 2009.
- [21] H. Tian, F. Mancilla-David, K. Ellis, E. Muljadi, and P. Jenkins, "A cell-to-module-to-array detailed model for photovoltaic panels," *Solar Energy*, 2012.
- [22] W. D. Soto, S. Klein, and W. Beckman, "Improvement and validation of a model for photovoltaic array performance," *Solar Energy*, 2006.
- [23] R. A. Messenger and J. Ventre, *Photovoltaic Systems Engineering, Third Edition*. CRC Press, 2010.
- [24] S. C. Bartling, S. Khanna, M. P. Clinton, S. R. Summerfelt, J. A. Rodriguez, and H. P. McAdams, "An 8mhz 75 μ a/mhz zero-leakage non-volatile logic-based cortex-m0 mcu soc exhibiting 100% digital state retention at v_{dd}= 0v with 400ns wakeup and sleep transitions," in *ISSCC*, 2013, pp. 432–433.
- [25] Y. Wang, Y. Liu, S. Li, D. Zhang, B. Zhao, M.-F. Chiang, Y. Yan, B. Sai, and H. Yang, "A 3 μ s wake-up time nonvolatile processor based on ferroelectric flip-flops," in *ESSCIRC*, 2012.
- [26] National Instrument, "NI-DAQ Family," Website: <http://www.ni.com/data-acquisition>.
- [27] Texas Instrument, "Datasheet of msp430fr573x mixed signal microcontrollers," Website: <http://www.ti.com/lit/ds/slas639j/slas639j.pdf>.
- [28] Y. Kim, N. Chang, Y. Wang, and M. Pedram, "Maximum power transfer tracking for a photovoltaic-supercapacitor energy system," in *ISLPED*, 2010.
- [29] National Renewable Energy Laboratory, "National Solar Radiation Data Base," Website: http://rredc.nrel.gov/solar/old_data/nsrdb.